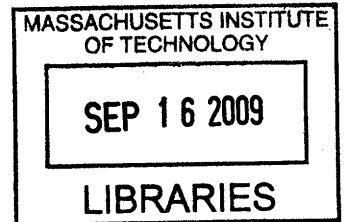


The Evaporation of Drops From Super-heated  
Nano-engineered Surfaces

by

Fiona Rachel Hughes



Submitted to the Department of Mechanical Engineering  
in partial fulfillment of the requirements for the degree of  
Bachelor of Science in Engineering as Recommended by the  
Department of Mechanical Engineering

at the

MASSACHUSETTS INSTITUTE OF TECHNOLOGY

June 2009

© Massachusetts Institute of Technology 2009. All rights reserved.

**ARCHIVES**

Author .....

Department of Mechanical Engineering  
May 15, 2009

Certified by .....

Kripa K. Varanasi  
Assistant Professor  
Thesis Supervisor

Accepted by .....

J. Lienhard V  
Collins Professor of Mechanical Engineering;  
Chairman, Undergraduate Thesis Committee



# The Evaporation of Drops From Super-heated Nano-engineered Surfaces

by

Fiona Rachel Hughes

Submitted to the Department of Mechanical Engineering  
on May 15, 2009, in partial fulfillment of the  
requirements for the degree of  
Bachelor of Science in Engineering as Recommended by the Department of  
Mechanical Engineering

## Abstract

In pool boiling and spray cooling the Leidenfrost point marks the transition from nucleate boiling, in which the evaporating liquid is in contact with the surface, and film boiling, in which a layer of vapor separates the fluid from the surface. For a single evaporating drop, the Leidenfrost point occurs when the capillary and gravitational forces are surpassed by the upward pressure of the escaping vapor. This thesis develops an analytical model to predict the Leidenfrost point for a microstructured surface. The microstructure consists of a regular array of square posts geometrically defined by aspect ratio and spacing ratio. The vapor pressure is modeled using the momentum equation for flow in a porous medium. Varying the geometric parameters indicated that aspect ratio and spacing ratio must be optimized to achieve the maximum Leidenfrost temperature. For a water drop evaporating from a silicon surface, the maximum Leidenfrost temperature is predicted to occur with an aspect ratio of 1.3 and a spacing ratio of 1.5.  $10 \mu\text{L}$  water drops were evaporated from a smooth surface made of silicon and porous surfaces made of aluminum oxide. The microstructure of the surfaces was different from that modeled, but increased wettability and higher Leidenfrost temperatures were observed as porosity increased. Recommendations for further research in this area are made.

Thesis Supervisor: Kripa K. Varanasi

Title: Assistant Professor



## Acknowledgments

First, I must express my appreciation for the enthusiastic and dedicated guidance of my thesis advisor, Professor Kripa Varanasi. His excitement for this subject is infectious and I have truly enjoyed working on this project.

I would like to thank Professor Ahmed Ghoniem, my academic advisor, for his advice and support during my time at MIT. It was his encouragement that motivated me to pursue a thesis in the first place.

This thesis could not have been completed without the help of Dr. Jim Bales and the MIT Edgerton Center. I'd like to thank Jim for his careful instruction in the use of the high speed camera and his generosity in allowing the use of Edgerton Center lab space. I also thank Professor Tonio Buonassissi and Allie Fecych for the use of laboratory equipment.

As I move on from MIT, I will not forget the support I have continuously received from my friends and housemates in the Women's Independent Living Group, particularly from the residents of the fourth floor. Lastly, I thank my parents, Faith and Tom Hughes, and my sister, Lyrana, for their tremendous love and encouragement. Their support not only got me into MIT, but through it, and I could not be more grateful.



# Contents

<b>1</b>	<b>Introduction</b>	<b>15</b>
1.1	Boiling Regimes . . . . .	15
1.2	Predicting the Leidenfrost Point . . . . .	17
1.3	Effects of Surface Roughness . . . . .	20
1.4	Objectives . . . . .	24
<b>2</b>	<b>Modeling the Leidenfrost Point on a Microstructured Surface</b>	<b>25</b>
2.1	Forces on an Evaporating Drop . . . . .	25
2.2	Vapor Pressure . . . . .	26
2.3	Wetting Pressure . . . . .	32
2.4	Force Comparison . . . . .	33
2.5	Chapter Summary . . . . .	36
<b>3</b>	<b>Evaporation of Drops from Porous Surfaces</b>	<b>39</b>
3.1	Experimental Set-up . . . . .	39
3.2	Boiling from Smooth Silicon . . . . .	41
3.3	Boiling from Porous Aluminum Oxide . . . . .	42
3.4	Drops Impinging From a Height . . . . .	45
3.5	Chapter Summary . . . . .	45
<b>4</b>	<b>Conclusions and Recommendations</b>	<b>47</b>





# List of Figures

1-1	Heat flux is plotted qualitatively as a function of surface superheat ??. D marks the critical heat flux. E marks the Leidenfrost point. . . . .	16
1-2	The vapor layer growth rate increases exponentially with temperature. The Leidenfrost point has been empirically identified to occur at 0.05 %/ms [3]. . . . .	18
1-3	Leidenfrost temperature increases with the impinging drops speed $u_0$ [2].	19
1-4	Surfaces with micro-indentations (micro-i) and micro-protrusions (micro- p) exhibited enhanced heat transfer over a smooth surface. Hysteresis was seen in the enhancement as the heat flux was increased from 0 $W/m^2$ to 500 $W/m^2$ and reduced again to 0 $W/m^2$ [7]. . . . .	21
1-5	In (a), 'x' represents solid steel evaporation and 'o' represents porous evaporation. The nucleate-to-film boiling transition occurs at a much higher superheat for the porous surface. (b) shows that as porosity increases, the initial levitation height decreases and the drop moves more quickly towards the surface [1]. . . . .	22
1-6	Hsieh et. al. tested microstructures from groove width $G = 120 \mu m$ to $G = 360 \mu m$ and from stud size $S = 160 \mu m$ to $S = 480 \mu m$ . [8]. .	23
1-7	Micro-textured surfaces exhibited higher film breakup temperatures than smooth silicon [8]. . . . .	23
2-1	An evaporating drop still in contact with the surface microstructure. .	26
2-2	The surface microstructure viewed from above. . . . .	27

2-3	$F_{vap}$ is plotted as a function of spacing ratio from $b/a = 0.25$ to $b/a = 25$ . . . . .	31
2-4	$F_{vap}$ is plotted against aspect ratio $h/a$ , which varies from 0.25 to 25. . . . .	32
2-5	$F_{vap}$ is plotted against drop volume $V$ . . . . .	33
2-6	Wetting force $F_{wet}$ is plotted against feature size $a$ and spacing ratio $b/a$ . . . . .	34
2-7	Wetting force $F_{wet}$ is shown as a function of feature size $a$ and drop volume $V$ . . . . .	34
2-8	The Leidenfrost temperature as a function of drop volume. As drop volume increases, the Leidenfrost temperature decreases. . . . .	35
2-9	The Leidenfrost temperature is plotted against spacing ratio and aspect ratio. For these conditions, the Leidenfrost temperature is maximized at a spacing ratio of 1.5 and an aspect ratio of 1.3 . . . . .	36
3-1	Plan view of the porous filters [10]. . . . .	40
3-2	(a) The experimental setup for the observation of interactions between the drop and the superheated surface. (b) The porous membranes were set on top of an Si wafer. . . . .	40
3-3	Drops evaporating from the silicon wafer at 190° C were in the transition regime. After impacting and recoiling a few times, the drop broke apart and nucleate boiling was observed. . . . .	41
3-4	At 200° C, film boiling is observed in drops evaporating from a smooth silicon surface. . . . .	42
3-5	Drops wetted the 40% porous surface at 205° C and evaporated via nucleate boiling. . . . .	43
3-6	Film boiling was observed in the 40% porous surface above 220° C. . . . .	44
3-7	At 230° C, impinging drops wetted the 50% porous surface and no recoil was observed. . . . .	44
3-8	Drops impinging on the 50% porous surface at 275° C evaporated via film boiling. . . . .	45

3-9 A drop impinging onto the silicon surface heated to 200° C quickly  
disintegrated. . . . . 46



# List of Tables

2.1	Surface and fluid properties used in equation 2.20. . . . .	31
2.2	Constant values and ranges of variation. . . . .	31
2.3	Surface and fluid properties used in equation 2.23. . . . .	33



# Chapter 1

## Introduction

### 1.1 Boiling Regimes

In pool boiling and spray cooling, four different regimes are observed as the temperature of the heated surface increases. The heat flux  $q$  from the surface to the evaporating liquid depends on the surface superheat  $\Delta T$ , the difference between the surface temperature and the boiling temperature of the liquid. Figure 1-1 illustrates these four regimes and the transitions between them. Below point B, natural convection is observed in the fluid and a few isolated bubbles may form. Point B marks the onset of nucleate boiling. During this phase, surface superheat causes vapor bubbles to form in irregular cavities on the surface. Surface cavities become activated when the available superheat can provide the gas pressure necessary to support a bubble of the same radius as the cavity. After this initial nucleation, a bubble grows until the buoyancy of the vapor is large enough to counteract the surface tension of the liquid and the bubble leaves the surface, which is rewetted by the liquid. Point D in Figure 1-1 marks the highest temperature at which the surface is always rewetted before another bubble is formed. The heat flux  $q$  is maximized at this point. This value of  $q$  is known as the critical heat flux.

Above point D is the regime known as transition boiling. Here, portions of the surface are blanketed with vapor and others are continually rewetted. Because heat transfer through vapor is much poorer than that through liquid, the heat flux de-

creases as more of the surface is covered in vapor. The heat flux reaches a minimum when the vapor layer becomes steady and continuous. This occurs at the Leidenfrost point, which is shown as point E.

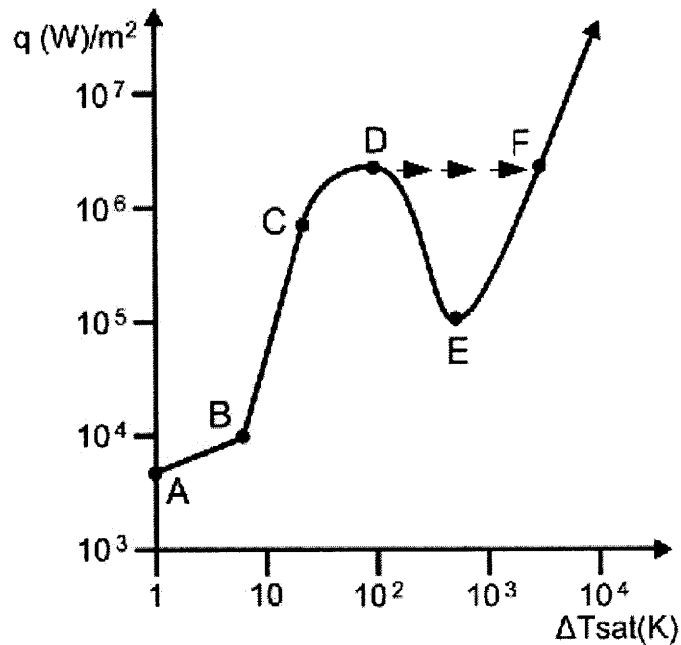


Figure 1-1: Heat flux is plotted qualitatively as a function of surface superheat  $\Delta T_{\text{sat}}$ . D marks the critical heat flux. E marks the Leidenfrost point.

Boiling is used extensively in power production, device cooling and in other applications where a high heat flux is desirable. To achieve the highest possible heat flux, is advantageous to operate such devices as close to the critical heat flux as possible. However, this can result in damage if the heat flux should surpass the critical heat flux. Although a slight increase in temperature above the critical heat flux point causes a reduction in heat flux, this decrease is not often observed in practice. In many heat transfer applications, the heat flux, rather than the surface superheat, is independently controlled. Such a system will transition directly from the nucleate regime to film boiling, resulting in a considerable rise in surface temperature. This increase can be on the order of hundreds of degrees K, and can easily melt or damage the solid surface. In Figure 1-1, the arrows trace the observed nucleate-to-film boiling transition.



To prevent damage from overheating, the heat flux from electronic devices and heat transfer mechanisms must be kept at or below the critical heat flux. This limit reduces the efficiency of nuclear steam cycles and the computational power of integrated circuits. A superwetting surface capable of maintaining contact with evaporating liquid above the conventional Leidenfrost point would allow these and other devices to be operated safely at higher temperatures.

## 1.2 Predicting the Leidenfrost Point

Given the damage that occurs when a system passes the Leidenfrost point, appreciable effort has been devoted to understanding the nucleate-to-film boiling transition. In [3], Bernardin and Mudawar propose a model for predicting the Leidenfrost point based on surface cavity size and bubble nucleation and growth. Bubbles are only nucleated in surface cavities whose radius  $R_b$  is

$$R_b = \frac{2\sigma}{p_{sat} - p_{ambient}} \quad (1.1)$$

in which  $\sigma$  is the surface tension of the liquid,  $p_{sat}$  is the saturation pressure at the surface temperature and  $p_{ambient}$  is the surrounding pressure. As surface superheat increases, the difference between  $p_{sat}$  and  $p_{ambient}$  becomes larger and the critical radius decreases. This results in the activation of smaller surface cavities and more rapid vapor production. The authors' model assumes that there is an exponential increase in the number of surface cavities with decreasing radius. Thus, as the temperature rises, exponentially more cavities are available for bubble nucleation. In addition, the enhanced heat transfer at higher superheat increases the bubble growth rate. The combination of these effects is seen in Figure 1-2, in which the average layer growth rate (defined as the change of the percent of solid-liquid interface covered by vapor ( $AB\%$ )) is plotted against interface temperature. The surface is polished aluminum and the liquid is water. For this system, Bernardin and Mudawar measured the Leidenfrost point to occur at  $162^\circ$  C. The vapor layer growth rate that corresponds to

the experimentally determined Leidenfrost point was identified as 0.05 %/ms, which is assumed to be independent of surface and liquid properties.

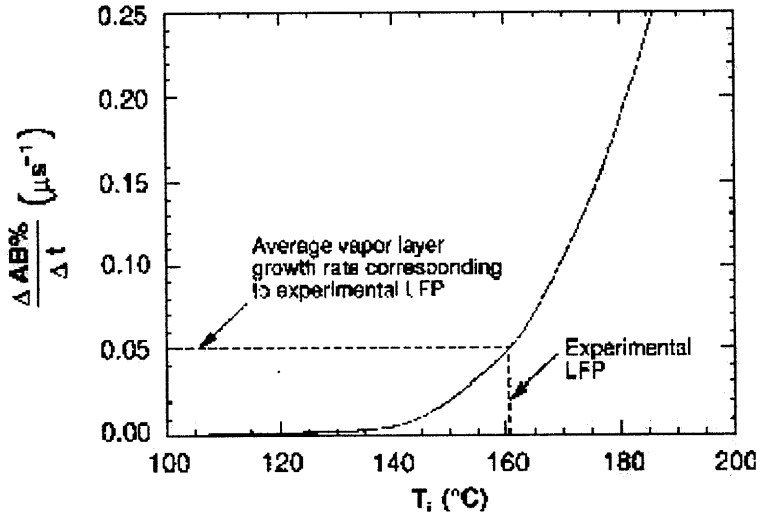


Figure 1-2: The vapor layer growth rate increases exponentially with temperature. The Leidenfrost point has been empirically identified to occur at 0.05 %/ms [3].

This theory is expanded for impinging droplets and sprays in [2]. The droplet impact pressure is approximated via one-dimensional elastic impact theory, and used to determine the fluid properties to be used in the previously discussed model. The experimental Leidenfrost temperatures observed for drops reaching the surface at various velocities are displayed in Figure 1-3, along with predictions from the model. Both experiment and theory indicate that the Leidenfrost temperature is higher for drops impinging at higher velocities. Experiments comparing particle blasted to polished surfaces showed a reduction in the Leidenfrost temperature for roughness features larger than the bubble nucleation cavities.

The evaporation process for droplets and sprays is studied empirically in [5] and [4]. High-speed photography was used to characterize droplet impact and evaporation for interfaces between the nucleate, transition and film boiling regions and for various values of Weber number, a ratio between droplet inertia  $\rho_{liq}u_0^2d_0$  and surface tension  $\sigma$ :

$$We = \frac{\rho_{liq}u_0^2d_0}{\sigma} \quad (1.2)$$

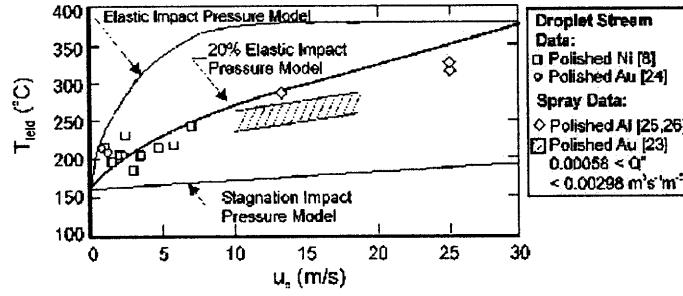


Figure 1-3: Leidenfrost temperature increases with the impinging drops speed  $u_0$  [2].

Weber numbers of 20, 60 and 220 were examined and the Leidenfrost point was found to be largely insensitive to changes in Weber number when drops impacted a polished surface. When drops impinged on surfaces of varying roughnesses, the Leidenfrost temperature was found to decrease with roughness. The high speed video revealed that the impinging drops were ruptured by the larger surface features which lowered the pressure beneath the spreading droplet. This result is opposite to that observed in sessile, or stationary, droplets. Surface features penetrate the vapor layer beneath sessile droplets, increasing solid-liquid contact and raising the Leidenfrost point.

The Leidenfrost point also depends on the size of the evaporating drop. Bianco et. al. examine the relationship between drop radius and vapor layer thickness for droplets boiling on solid surfaces [6]. They find that the thickness of the vapor layer always decreases as drops evaporate, but that the exact relationship depends on the size of the drop. Above the capillary length

$$a = \sqrt{\frac{\sigma}{\rho g}} \quad (1.3)$$

the vapor layer thickness  $e$  scales as drop radius  $R^{0.5}$ , where  $R$  is drop radius. Below the capillary length,  $e$  scales as  $R^{1.3}$ . The authors attribute this acceleration to a change in the way the liquid is evaporated. For drops larger than the capillary length, all evaporation occurs at the bottom of the drop and all vapor flows into the vapor layer. Liquid evaporates from the entire surface of smaller drops, but only vapor from

underneath the drop contributes to the vapor layer.

### 1.3 Effects of Surface Roughness

Surface characteristics such as roughness and porosity have been found to affect the boiling of sessile (stationary) as well as impinging drops. Hysteresis is observed in the heating and cooling curves for the spray cooling of rough surfaces in [7]. Heat flux and surface superheat are recorded for a smooth surface (feature size  $0.3 \mu\text{m}$ ), a micro-indented surface (feature size  $\approx 2\mu\text{m}$ ), and a micro-protruded surface (feature size  $\approx 15\mu\text{m}$ ). The heat transfer coefficients observed for the indented and protruded surfaces were uniformly higher than that of the smooth surface, reaching values 1.52 and 2.15 times greater for a heat flux of  $500 \text{ W}/\text{m}^2$ . This impressive increase is attributed to the wider range of cavity sizes present on the microstructured surfaces, which increases the number of nucleation sites. When surface heat flux was systematically increased and decreased, the microstructured surfaces exhibited greater hysteresis during the cool down phase. Lower superheat was needed to achieve the same heat flux from the microstructured surface due to the number of cavities which trapped vapor at higher heat fluxes and stayed activated as the heat flux was reduced. The hysteresis effect and increase in heat transfer coefficient can be seen in Figure 1-4. The ratio of the heat transfer coefficients for the microstructured and plain surfaces are plotted as functions of heat flux.

Avedisian and Koplik [1] develop a model for the film boiling of sessile drops on porous surfaces using the momentum equation for flow in a porous medium and a mass balance between the vapor layer and the drop. They determine that the Leidenfrost point increases with increasing surface porosity. This result was supported by experiments using methanol drops on polished stainless steel and alumina silicate surfaces of various porosities. Figure 1-5(a) shows the droplet evaporation time relative to surface temperature. The drastic increase corresponding to the transition from nucleate to film boiling occurred at 448 K for solid stainless steel and at 570 K for a surface with porosity  $\phi = 10\%$ . A 40% porous material was also tested, but the

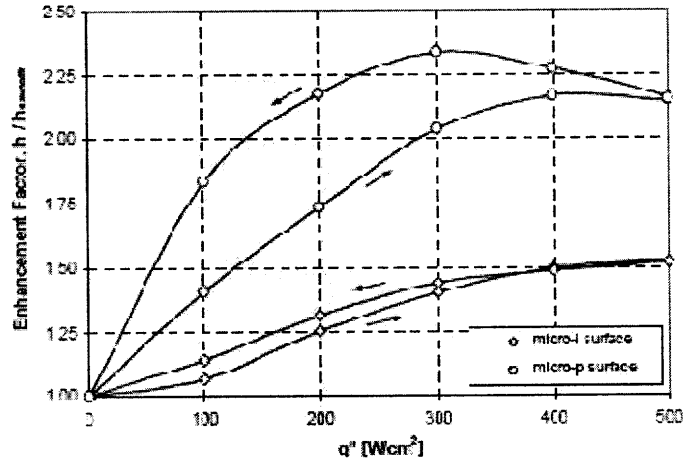


Figure 1-4: Surfaces with micro-indentations (micro-i) and micro-protrusions (micro-p) exhibited enhanced heat transfer over a smooth surface. Hysteresis was seen in the enhancement as the heat flux was increased from  $0 W/m^2$  to  $500 W/m^2$  and reduced again to  $0 W/m^2$  [7]

apparatus could not heat the surface to its Leidenfrost temperature, which is greater than 620 K.

This model indicates that porosity reduces evaporation time even within the film boiling regime. The vapor layer underneath the drop seeps into the porous surface layer, bringing the bottom of the drop closer to the top of the pores. This process will eventually result in the drops making contact and wetting the surface, as shown in Figure 1-5(b).

Hsieh et. al. discuss the effects of a regular microstructure on the evaporation of sessile drops and liquid sprays [8]. They used deep reactive ion etching (DRIE) to etch grooves  $350 \mu m$  into the silicon wafer, in the patterns shown in Figure 1-6. The groove width  $G$  and stud width  $S$  of the microstructure were varied independently. The goal of the microstructuring was to enhance the wettability of the Si surface, which is typically not very wettable by water. The Bond number,

$$Bo = \frac{G}{\sqrt{\frac{\sigma}{(\rho_{liq} - \rho_{vap})g}}} \quad (1.4)$$

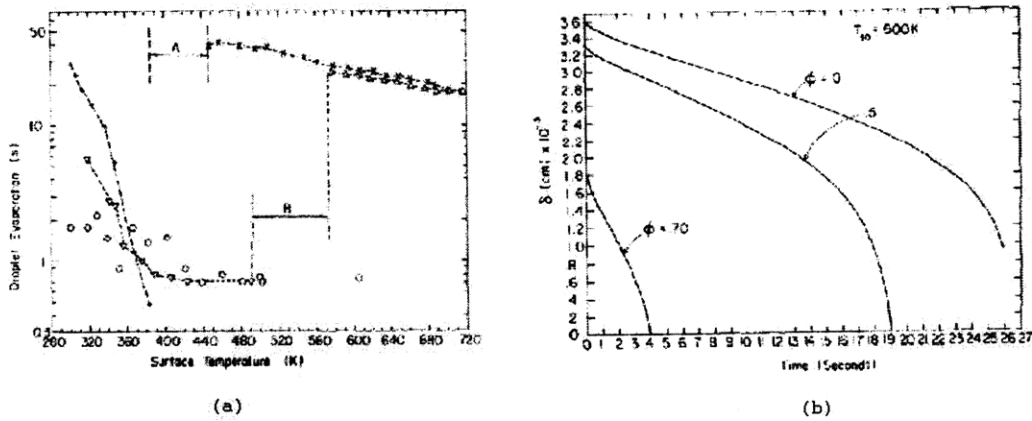


Figure 1-5: In (a), 'x' represents solid steel evaporation and 'o' represents porous evaporation. The nucleate-to-film boiling transition occurs at a much higher superheat for the porous surface. (b) shows that as porosity increases, the initial levitation height decreases and the drop moves more quickly towards the surface [1].

a ratio between the gravitational force and surface tension, and the groove bottom surface area were used to characterize the various microstructures. Sessile drops were evaporated from these surfaces, as well as a plain silicon surface, at  $80^\circ C$ . The capillary forces causing the liquid to spread into a thin film were largest for the  $120G \times 160S$  surface because of the narrow grooves, resulting in the shortest evaporation time. The capillary forces from the  $360G \times 480S$  surface were not enough to keep the drop from breaking into several smaller sections. This increased the film thickness and evaporation time, but the drops still evaporated more quickly than those placed on plain silicon.

These surfaces were also tested under a spray of droplets at superheated temperatures. The textured surfaces raised the film breakup point from below  $80^\circ C$  to about  $110^\circ C$ , and showed higher heat fluxes during thin film evaporation and after film breakup, as shown in Figure 1-7. The droplets were between  $75$  and  $100 \mu m$ , slightly smaller than the surface features, so the effects observed near the Leidenfrost point in [1] could not be studied.

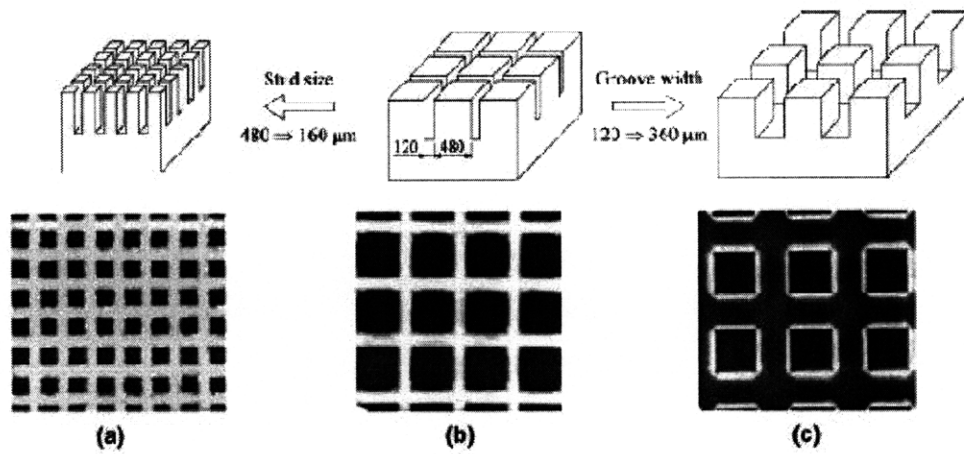


Figure 1-6: Hsieh et. al. tested microstructures from groove width  $G = 120 \mu m$  to  $G = 360 \mu m$  and from stud size  $S = 160 \mu m$  to  $S = 480 \mu m$ . [8].

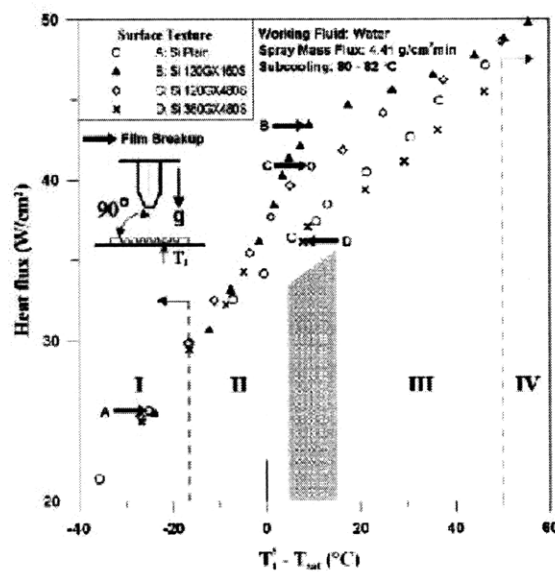


Figure 1-7: Micro-textured surfaces exhibited higher film breakup temperatures than smooth silicon [8].

## 1.4 Objectives

The goal of this thesis is to identify a design space for superwetting surfaces. The effect of regular microstructures (similar to those studied in [8]) on droplet wettability at superheated temperatures will be investigated analytically. A force balance between the capillary pressure, droplet weight and vapor layer pressure will be used to predict the range of aspect and spacing ratios and feature size that result in increased wettability. This analysis is discussed in Chapter 2.

Boiling experiments will be performed to gain further insight into the effect of porosity on the Leidenfrost point. The evaporation of impinging drops from smooth silicon as well as from commercially available surfaces of 40% and 50% porosity will be observed via high speed camera and thermal measurement systems. The trends predicted by the model will be compared to the experimental data. The results of these experiments are presented in Chapter 3. Recommendations for further research are given in Chapter 4.



# Chapter 2

## Modeling the Leidenfrost Point on a Microstructured Surface

### 2.1 Forces on an Evaporating Drop

There are three forces acting on a drop evaporating from a superheated surface. The weight of the drop and the capillary force pull the drop towards the surface, while the pressure exerted by the escaping vapor repels the drop from the surface. The balance of these forces determines whether a drop will wet the surface or whether it will be stably levitated above the vapor layer.

A drop evaporating from a smooth surface reaches the Leidenfrost point when the vapor beneath the drop forms a continuous and stable layer. The situation is more complex for microstructured surfaces because the liquid will remain in contact with the surface until the vapor layer becomes thicker than the surface features. Figure 2-1 shows a drop still in contact with the regular posts that make up the microstructure that will be examined here. The vapor layer has reached the thickness of the microstructure, but has not separated the drop from the surface. The square posts with side length  $a$  and height  $h$  are spaced a distance  $b$  apart.  $R_0$  is the radius of the area of contact between the drop and the surface. A top view of the structure can be seen in Figure 2-2.

During this intermediate regime, heat is transferred through the vapor layer as well

as through the posts that are in contact with the drop. A one-dimensional model of the forces in this regime is developed below. These forces depend on the geometry of the microstructure, the properties of the fluid and the surface, and the size of the drop.

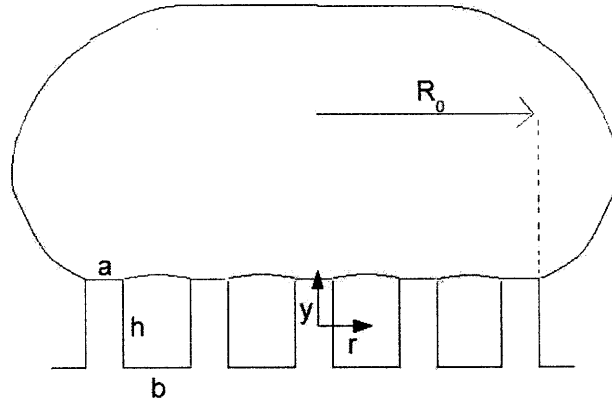


Figure 2-1: An evaporating drop still in contact with the surface microstructure.

## 2.2 Vapor Pressure

The one dimensional momentum equation for flow in a porous medium is

$$\frac{d^2u}{dy^2} = \frac{\epsilon}{\mu} \frac{dP}{dr} + \frac{\epsilon u}{K} \quad (2.1)$$

in which  $u$  is vapor velocity,  $P$  is pressure,  $\mu$  is vapor viscosity,  $\epsilon$  and  $K$  are the surface porosity and permeability, respectively, and  $y$  and  $r$  are as shown in Figure 2-2. This equation is used to calculate the pressure exerted on the drop by the escaping vapor. The drop is assumed to be stably levitated at the top of the posts, as illustrated in Figure 2-2. The escaping vapor flows radially outward from the drop. The average velocity of the vapor at radius  $r$  is determined by the rate of evaporation from the bottom of the drop. The heat flux  $q$  is taken to be simple conduction from the

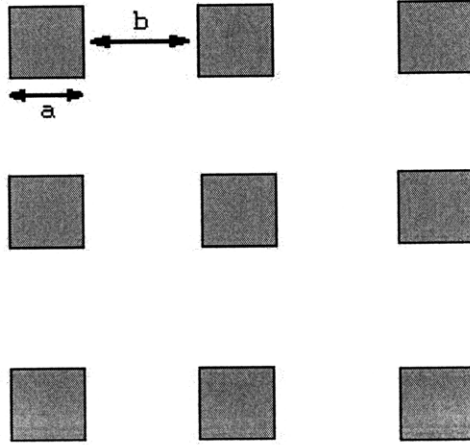


Figure 2-2: The surface microstructure viewed from above.

substrate to the drop and is given by

$$q = \frac{\Delta T k_{eff}}{h} \quad (2.2)$$

in which  $\Delta T$  is the surface superheat,  $h$  is the height of the posts, and  $k_{eff}$  is the effective thermal conductivity of the microstructure.  $k_{eff}$  depends on the spacing ratio  $b/a$  as well as the thermal conductivity of the vapor,  $k_{vap}$  and of the substrate,  $k_{surf}$ :

$$k_{eff} = k_{vap} \frac{\left(1 + \frac{b}{a}\right)^2 - 1}{\left(1 + \frac{b}{a}\right)^2} + k_{surf} \frac{1}{\left(1 + \frac{b}{a}\right)^2} \quad (2.3)$$

A mass balance between the evaporating and escaping vapor defines the relation between the average vapor velocity  $u_{ave}$  and the heat flux  $q$  to be

$$A_{flow} \rho_{vap} u_{ave} = A_{contact} \frac{q}{h_{fg}} \quad (2.4)$$

in which  $\rho_{vap}$  is the density of the vapor and  $h_{fg}$  is the latent heat of vaporization. In this case, equation 2.4 can be rewritten as

$$(2\pi rh)\rho_{vap}u_{ave} = \left(\pi r^2\right)\frac{q}{h_{fg}} \quad (2.5)$$

Combining equations 2.2 and 2.5 yields the following relation for  $u_{ave}$ :

$$u_{ave} = \frac{\Delta T k_{eff}}{2h_{fg}\rho_{vap}h^2}r \equiv \Psi r \quad (2.6)$$

The flow of the escaping vapor is modeled as laminar flow between two parallel plates a distance  $h$  apart. The substrate at the bottom of the microstructure is the lower plate and the drop itself is the upper plate. The velocity profile of fluid in this situation is

$$\frac{u}{u_{ave}} = \frac{3}{2} \left[ 1 - 4 \left( \frac{y}{h} \right)^2 \right] \quad (2.7)$$

When the definition of  $u_{ave}$  given in equation 2.6 is included,

$$u = \frac{3}{2}\Psi r \left[ 1 - 4 \left( \frac{y}{h} \right)^2 \right] \quad (2.8)$$

$$\frac{du}{dy} = -\frac{12\Psi r y}{h^2} \quad (2.9)$$

$$\frac{d^2u}{dy^2} = -\frac{12\Psi r}{h^2} \quad (2.10)$$

Substituting the 2nd derivative of vapor velocity  $u$ , equation 2.10, and the average velocity  $u_{ave}$  into the momentum equation 2.1 results in the following relation between vapor pressure  $P$  and contact radius  $r$ :

$$\frac{dP}{dr} = -\mu\Psi r \left( \frac{12}{\epsilon h^2} + \frac{1}{K} \right) \quad (2.11)$$

Integrating this equation between position  $r$  and patch radius  $R_0$  results in a quadratic relation between radial position and pressure difference:

$$P(r) - P_\infty = \frac{\mu\Psi}{2} \left( \frac{12}{\epsilon h^2} + \frac{1}{K} \right) (R_0^2 - r^2) \quad (2.12)$$

in which  $P_\infty$  is atmospheric pressure at the edge of the drop. The total force on the drop from the escaping vapor is found when equation 2.12 is integrated over the contact area. This force

$$F_{vap} = \frac{\mu\Psi\pi}{2} \left( \frac{12}{\epsilon h^2} + \frac{1}{K} \right) R_0^4 \quad (2.13)$$

is explicitly dependent on height  $h$  and patch radius  $R_0$ , which can be approximated as a function of the drop volume  $V$ , fluid density  $\rho$ , surface tension  $\sigma$  and gravitational acceleration  $g$  [6]:

$$R_0 = \frac{\left( \frac{3V}{4\pi} \right)^{2/3}}{\left( \frac{\sigma}{\rho g} \right)^{1/2}} \quad (2.14)$$

Equation 2.14 is a relation developed for levitated drops. Immediately before levitation, when the drop is still in contact with the top of the microstructure, it is assumed that the contact radius approaches this value.

Because permeability  $K$ , porosity  $\epsilon$ , and the variable  $\Psi$  defined above vary with feature size  $a$  and spacing ratio  $b/a$ ,  $F_{vap}$  also depends on the geometry of the surface microstructure. Porosity  $\epsilon$  is defined as the ratio between the open area available for vapor flow and the total cross-sectional area. This ratio is dependent only on the microstructural spacing ratio  $b/a$ :

$$\epsilon = \frac{A_{flow}}{A_{total}} = \frac{b/a}{1 + b/a} \quad (2.15)$$

Permeability  $K$  is calculated according to the relationship given for open rectangular grooves in [9],

$$K = \frac{2\epsilon (r_{h,b})^2}{f \cdot \text{Re}} \quad (2.16)$$

in which the hydraulic radius  $r_{h,b}$  is given as

$$r_{h,b} = \frac{2bh}{b + 2h} \quad (2.17)$$

while the frictional coefficient  $f \cdot Re$  is approximated by the empirical correlation [9]

$$f \cdot Re = 14 + 10e^{-3b/h} \quad (2.18)$$

The combination of equations 2.16 through 2.18 results in

$$K = 2 \left( \frac{b/a}{1 + b/a} \right) \left( \frac{2bh}{b + 2h} \right)^2 \left( \frac{1}{14 + 10e^{-3b/h}} \right) \quad (2.19)$$

When the above values for permeability  $K$ , porosity  $\epsilon$ , and the variable  $\psi$  are substituted into equation 2.13, the vapor force  $F_{vap}$  is found to be

$$F_{vap} = \frac{\pi\mu}{4} \left( \frac{\Delta T}{h_{fg}\rho_{vap}} \right) \left[ k_{vap} \frac{(1 + \frac{b}{a})^2 - 1}{(1 + \frac{b}{a})^2} + k_{surf} \frac{1}{(1 + \frac{b}{a})^2} \right] \times \left[ \frac{12(\frac{b}{a})}{1 + \frac{b}{a}} + \frac{1}{8} \left( 1 + \frac{b}{a} \right) \frac{(\frac{b + 2h}{a})^2}{(\frac{b}{a})^3} (14 + 10e^{-3b/h}) \right] \left( \frac{R_0}{h} \right)^4 \quad (2.20)$$

This relation was modeled in MATLAB as a function of the geometric parameters  $h/a$  and  $b/a$ , and drop volume  $V$ . Properties of the fluid and the surface were kept constant at the values shown in Table 2.1. Drop properties are those of water at 100° C; surface properties are those of silicon dioxide (SiO<sub>2</sub>). Vapor force  $F_{vap}$  is plotted against each variable parameter ( $h/a$ ,  $b/a$ , and  $V$ ) in Figures 2-3 through 2-5. The parameters not being varied were kept constant at the values presented in Table 2.2.

In Figure 2-3, the spacing ratio  $b/a$  is increased from 0.25 to 25.  $F_{vap}$  monotonically decreases with spacing ratio. When  $b/a$  is small,  $F_{vap} \propto (b/a)^{-3}$ . Starting around  $b/a = 2.5$ , the downward slope begins to level off and  $F_{vap}$  approaches a constant value of  $10^{-4}$ .

Figure 2-4 illustrates  $F_{vap}$  as a function of aspect ratio  $h/a$ . At small aspect ratios,  $F_{vap}$  is constant at  $10^{-4}$ . Starting around an aspect ratio of 1,  $F_{vap}$  begins to increase as  $(h/a)^2$ . In the limit of small aspect ratio and large spacing ratio, the

Parameter	Value	Parameter	Value
$\mu$	$1.27 \times 10^{-5} \text{ Ns/m}$	$\Delta T$	$30^\circ\text{C}$
$\rho_{vap}$	$0.6 \text{ kg/m}^3$	$k_{vap}$	$0.68 \text{ W/mK}$
$h_{fg}$	$2258 \text{ kJ/kg}$	$k_{surf}$	$1.2 \text{ W/mK}$
$h$	$10 \text{ }\mu\text{m}$		

Table 2.1: Surface and fluid properties used in equation 2.20.

Parameter	Static Value	Range
$h/a$	2.5	0.25 to 25
$b/a$	2.5	0.25 to 25
$V$	$1 \text{ }\mu\text{L}$	$0.1 \text{ }\mu\text{L}$ to $10 \text{ }\mu\text{L}$

Table 2.2: Constant values and ranges of variation.

microstructure becomes a smooth surface.

The effect of varying drop volume is shown in Figure 2-5. The vapor force  $F_{vap}$  increases as  $V^{4/3}$ . This indicates that the pressure on the bottom of the drop is proportional to  $V^{2/3}$  and actually reduces as the drop increases. This is consistent with the previous observation [6] that extremely drops require higher surface superheats for levitation. The model assumes that all evaporation occurs at the bottom of the drop and no convection occurs in the drop liquid.

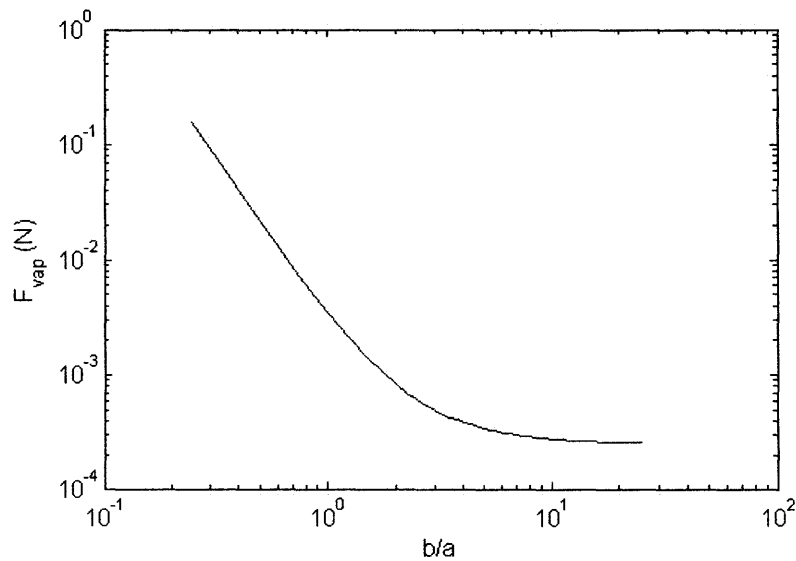


Figure 2-3:  $F_{vap}$  is plotted as a function of spacing ratio from  $b/a = 0.25$  to  $b/a = 25$ .

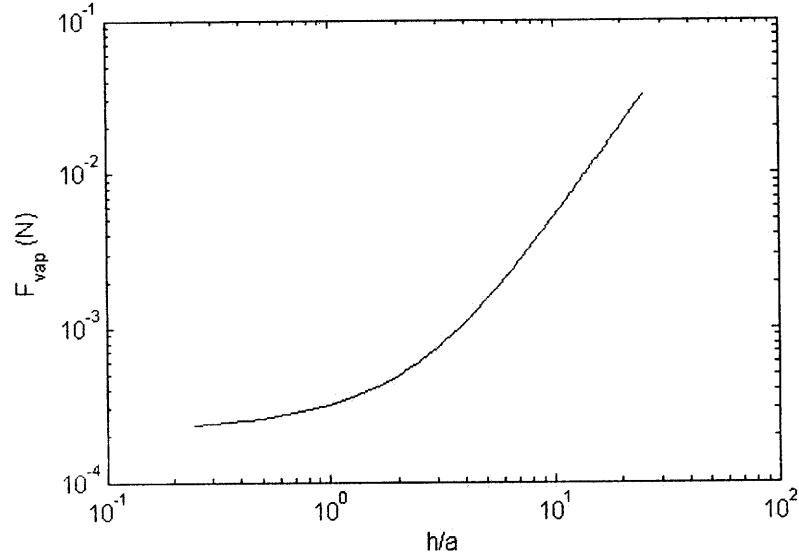


Figure 2-4:  $F_{vap}$  is plotted against aspect ratio  $h/a$ , which varies from 0.25 to 25.

## 2.3 Wetting Pressure

For a stationary interface, the capillary pressure  $p_c$  is defined by the interface area  $A$  and perimeter  $P$  and liquid contact angle  $\theta$  and surface tension  $\sigma$ :

$$p_c A = \sigma \cos \theta P \quad (2.21)$$

For the microstructure geometry, the capillary pressure  $p_c$  is

$$p_c = \frac{4\sigma \cos \theta}{\left[ \left(1 + b/a\right)^2 - 1 \right] a} \quad (2.22)$$

as given in [11]. The total wetting force

$$F_{wet} = \frac{4\sigma \cos \theta}{\left[ \left(1 + b/a\right)^2 - 1 \right] a} (\pi R_0^2) + V \rho_{liq} g \quad (2.23)$$

is the sum of the capillary force and gravity. The wetting force depends on the feature size  $a$ , spacing ratio  $b/a$  and drop volume  $V$ . The variation of  $F_{wet}$  with these



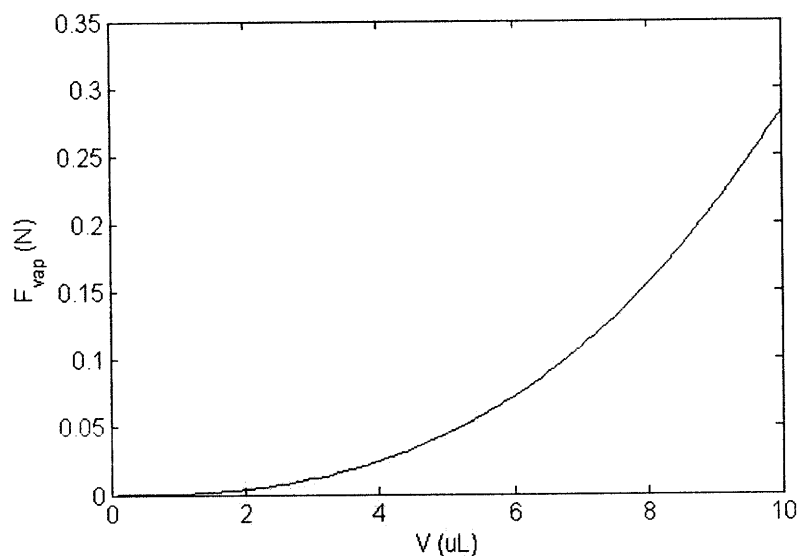


Figure 2-5:  $F_{vap}$  is plotted against drop volume  $V$ .

Parameter	Value	Parameter	Value
$\sigma$	0.0589 Nm	$\theta$	30°
$\rho_{liq}$	1000 kg/m <sup>3</sup>	$g$	9.8 m/s <sup>2</sup>

Table 2.3: Surface and fluid properties used in equation 2.23.

parameters is shown in Figures 2-6 and 2-7. All other terms were kept constant at the values recorded in Table 2.3. The same variable ranges shown in Table 2.2 were used. Feature size  $a$  is increased from 25 nm to 100  $\mu\text{m}$ . In Figure 2-6,  $F_{wet}$  monotonically decreases with feature size  $a$  and with spacing ratio  $b/a$ . For most of the range of  $a$  under consideration, the capillary force is dominant. But as  $a$  increases, the gravity term in equation 2.23 begins to become important and the negative slope decreases. The same trend is observed in Figure 2-7 and is most noticeable for smaller drop volumes.

## 2.4 Force Comparison

When the wetting force  $F_{wet}$  is larger than the vapor force  $F_{vap}$ , the drop will wet the surface microstructure and the system will be below the Leidenfrost point. In this

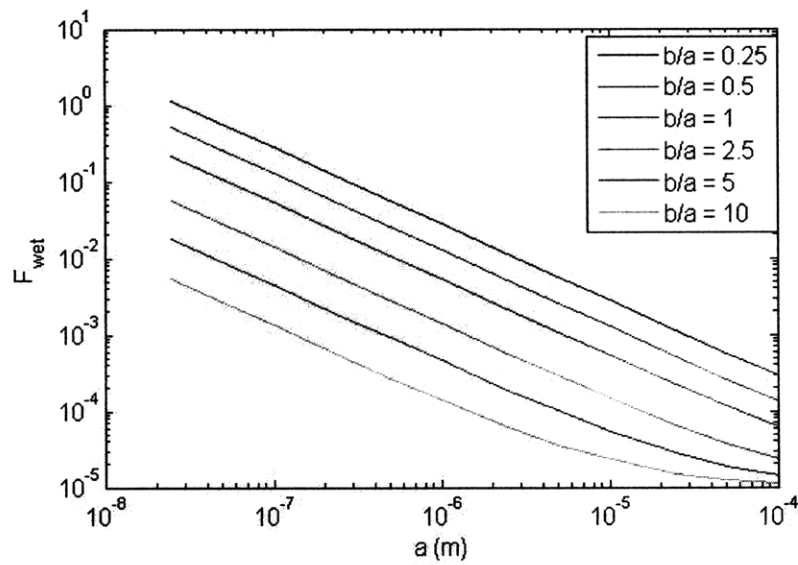


Figure 2-6: Wetting force  $F_{wet}$  is plotted against feature size  $a$  and spacing ratio  $b/a$ .

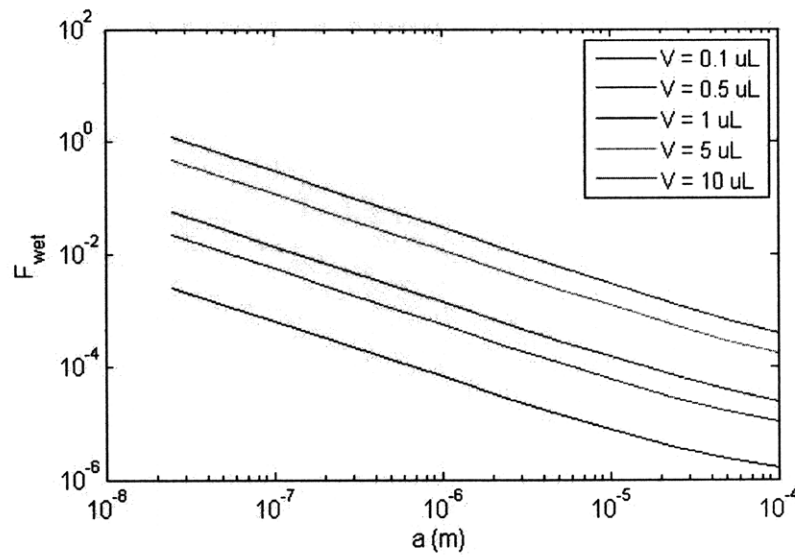


Figure 2-7: Wetting force  $F_{wet}$  is shown as a function of feature size  $a$  and drop volume  $V$ .

model, surface tension  $\sigma$  is assumed to be a constant, independent of temperature, and therefore  $F_{wet}$  does not depend on surface temperature.  $F_{vap}$  increases linearly with surface superheat  $\Delta T = T_{surface} - T_{critical}$ . The Leidenfrost point occurs when these  $F_{vap}$  surpasses  $F_{wet}$ . By setting  $F_{vap}$  equal to  $F_{wet}$ , the Leidenfrost temperature can be extracted. Figures 2-8 and 2-9 plot the predicted Leidenfrost temperature as functions of drop volume and microstructure geometry.

The effect of changing the drop volume  $V$  can be seen in Figure 2-8. While the two terms in the wetting force  $F_{wet}$  (as described by equation 2.23) depend on  $V$  and  $V^{2/3}$ , the vapor force  $F_{vap}$  goes as  $V^{4/3}$ . Therefore, the Leidenfrost temperature is reduced as  $V$  increases. These relationships are expected to become more complex at small drop volumes when the drop is more spherical and equation 2.14 is less accurate. Additionally, at large volumes the vapor layer can become unstable and divide the drop into several smaller drops [6].

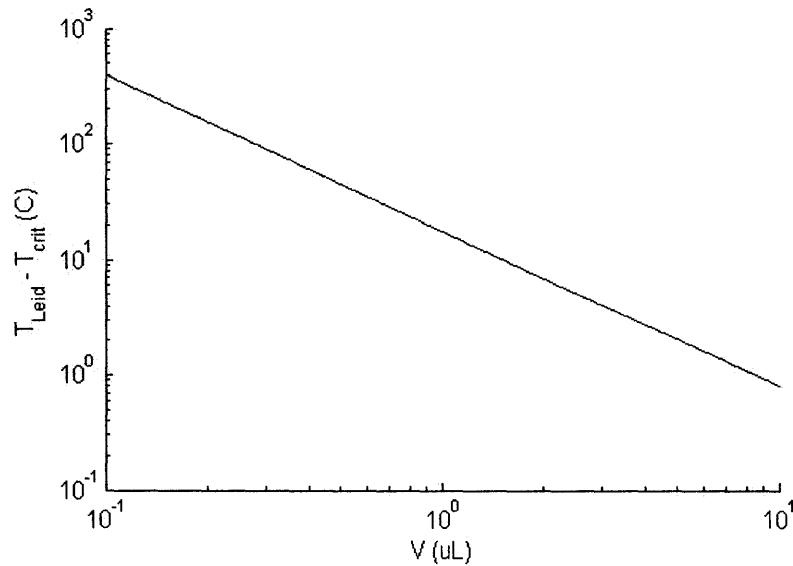


Figure 2-8: The Leidenfrost temperature as a function of drop volume. As drop volume increases, the Leidenfrost temperature decreases.

Spacing ratio  $b/a$  and aspect ratio  $h/a$  are varied in Figure 2-9. The spacing ratio is plotted on the abscissa while the several contours show different aspect ratios. The Leidenfrost temperature is low at extreme values of the spacing ratio and exhibits a maximum within the range plotted. The spacing ratio resulting in a maximum

Leidenfrost temperature shifts upwards as the aspect ratio increases. Under the conditions modeled here, the maximum Leidenfrost temperature occurs at  $h/a = 1.3$  and  $b/a = 1.5$ . This point will vary with the physical properties of the surface and the evaporating liquid.

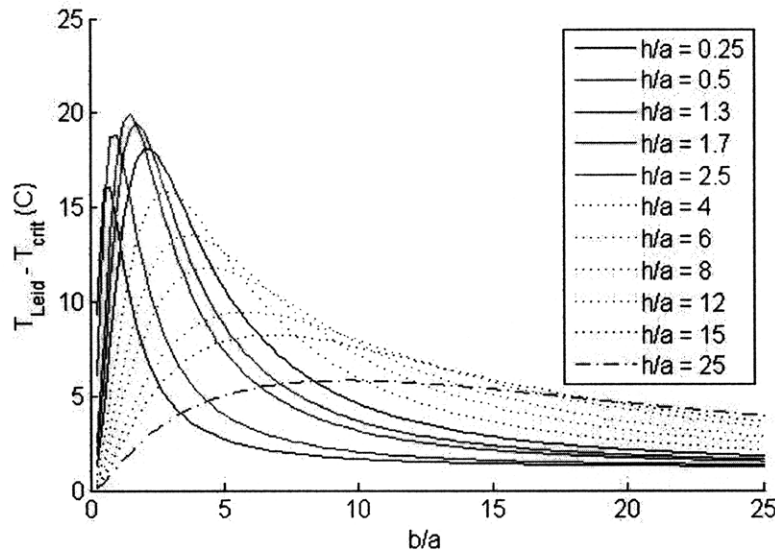


Figure 2-9: The Leidenfrost temperature is plotted against spacing ratio and aspect ratio. For these conditions, the Leidenfrost temperature is maximized at a spacing ratio of 1.5 and an aspect ratio of 1.3

## 2.5 Chapter Summary

In this chapter, the forces acting on a drop evaporating from a nano-engineered surface were formulated as functions of microstructure geometry, drop volume and the physical properties of the system. The surfaces textures modeled consisted of a regular array of square posts defined by feature size  $a$ , distance between posts  $b$ , and feature height  $h$ . This microstructured was approximated as a porous media using empirical correlations from [9].  $F_{vap}$  was developed using the momentum equation for flow in a porous media. The velocity profile within the microstructure was approximated as laminar flow between two plates. The relative magnitudes of the upwards vapor force  $F_{vap}$  and the downwards wetting force  $F_{wet}$  determine the Leidenfrost

temperature. The spacing ratio  $b/a$  and the aspect ratio  $h/a$  of the microstructure were varied and the conditions necessary to reach a maximum Leidenfrost temperature were identified. For water evaporating from a silicon dioxide surface, the highest Leidenfrost temperature occurred at  $b/a = 1.5$  and  $h/a = 1.3$ .



# Chapter 3

## Evaporation of Drops from Porous Surfaces

### 3.1 Experimental Set-up

High speed video was used to capture the evaporation of impinging drops from superheated surfaces of varying porosity. Evaporation from commercially available inorganic membrane filters of 40% and 50% porosity was compared to evaporation from a smooth silicon wafer that was 300  $\mu\text{m}$  thick. Although the bulk of the wafer was pure silicon, all surfaces exposed to air had a layer of silicon dioxide. Both porous membranes were 60  $\mu\text{m}$  thick and fabricated from aluminum oxide. The 40% porous surface has circular pores that are 0.1  $\mu\text{m}$  in diameter and has  $10^{10}$  pores/ $\text{cm}^2$ . The pores of the 50% porous surface are 0.02  $\mu\text{m}$  in diameter and there are  $10^{11}$  pores/ $\text{cm}^2$ . Figure 3-1 is a magnified plan view of the structure of the aluminum oxide membranes. Unlike the surfaces modeled in Chapter 2, these pores are not interconnected. Each pore is self-contained and extends through the entire thickness of the wafer.

The wafers were placed on a ceramic hot plate as shown in Figure 3-2. The wafer temperature was measured via a T-type thermocouple. The porous membranes were placed on top of silicon wafers and were assumed to be at approximately the temperature of the wafers. A precision micropipette was used to deposit 10  $\mu\text{L}$  drops of deionized water onto the surfaces from a height of 1 cm. The impact of the drops

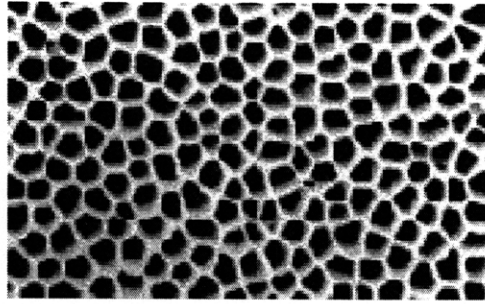


Figure 3-1: Plan view of the porous filters [10].

was recorded with a high speed video camera at 10,000 frames per second. The temperature was increased from 100° C until the Leidenfrost point was reached. Droplet impacts were recorded both below and above the Leidenfrost point. A sequence of still images depicting drop impact was extracted from each video. These are presented in Figures 3-3 through 3-9.

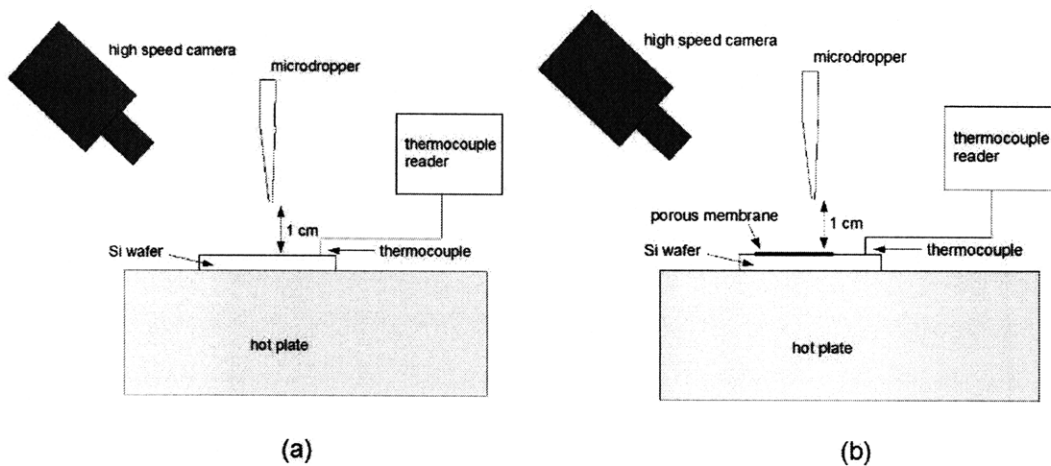


Figure 3-2: (a) The experimental setup for the observation of interactions between the drop and the superheated surface. (b) The porous membranes were set on top of an Si wafer.



## 3.2 Boiling from Smooth Silicon

When the temperature of the silicon wafer surface was at approximately 190° C, the impinging drops exhibited transition regime characteristics. Figure 3-3 shows the progression of the drop beginning shortly before it first impacted the surface. Upon impact, the drop flattened and expanded as visible in the second frame, about 5 ms after initial surface impact. During recoil, the drop became partially pinched, but did not separate into multiple droplets and did not lose contact with the surface. The maximum vertical elongation of the drop was reached 23.3 ms after surface impact, in the fourth frame. After this recoil from the surface, the drop was alternately elongated and flattened until about 65 ms past impact (frame eight of Figure 3-3), when nucleate boiling began at the bottom of the drop.

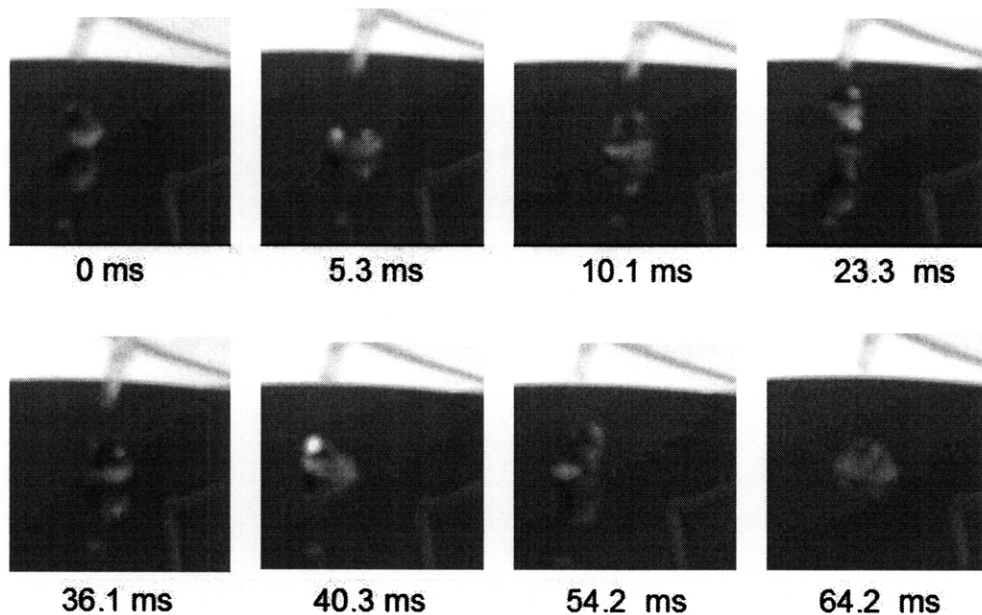


Figure 3-3: Drops evaporating from the silicon wafer at 190° C were in the transition regime. After impacting and recoiling a few times, the drop broke apart and nucleate boiling was observed.

Figure 3-4 shows the trajectory of a drop evaporating from smooth silicon at 200° C. As before, maximum flattening was reached approximately 5 ms after surface impact and the drop became pinched during recoil. The drop lost contact with the

surface 25 ms after initial contact and divided into two drops about 28 ms after initial contact, as visible in frame five. The two drops were recombined only 4 ms after separation and did not re-separate. The relative movement of different parts of the drop caused its shape to oscillate while it was levitated. Total levitation time was 35.3 ms. The drop re-impacted the surface 60.1 ms after its first contact and took 6 ms, slightly longer than at the first impact, to become maximally flattened. The drop repeated this process with diminished shape oscillations, but did not stabilize on the surface and eventually bounced off of the hot plate. This indicates that the Leidenfrost temperature for water evaporating from smooth silicon is between 190° C and 200° C.

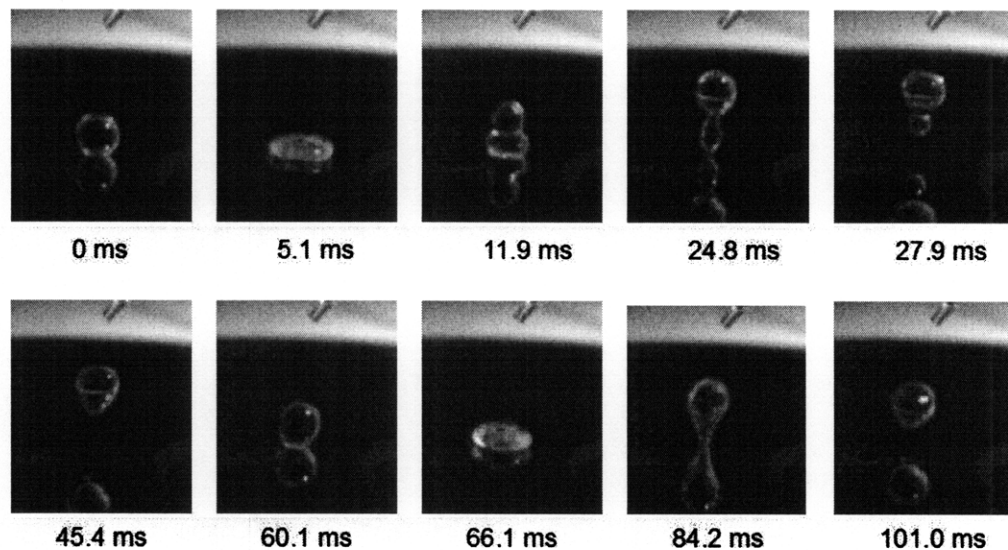


Figure 3-4: At 200° C, film boiling is observed in drops evaporating from a smooth silicon surface.

### 3.3 Boiling from Porous Aluminum Oxide

The 40% porous aluminum oxide membrane exhibited nucleate boiling at 205° C, roughly 10° C above the Leidenfrost point observed for smooth silicon. After initial impact, the reached maximum spreading 4.4 ms after initial impact. The shape variations were not as dramatic as those seen at 190° C for the silicon surface, but

continued for over 70 ms.

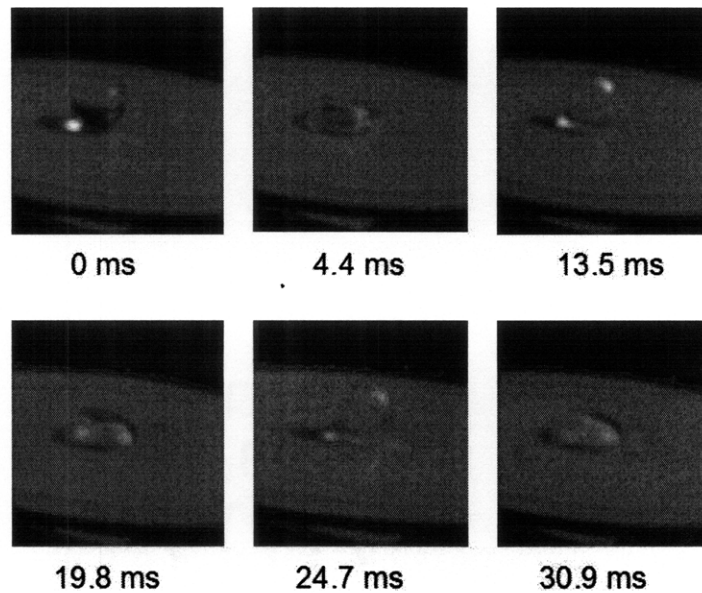


Figure 3-5: Drops wetted the 40% porous surface at 205° C and evaporated via nucleate boiling.

Film boiling was observed on the 40% porous surface when temperatures exceeded 220° C. Figure 3-6 presents the drop's progression. Maximum flattening was reached 5.3 ms after surface contact, and the drop lost contact with the surface nearly 13 ms after first contact. The drop did not become pinched, but did change shape while levitated above the surface. Frames four through seven show the drop oscillating between elongated and flattened shapes. The second impact occurred 58.5 ms after the first, and maximum flattening occurred only 3.9 ms after the second impact. The drop was out of contact with the surface for 45.7 ms. Even after several impacts, the drop was unable to wet the surface and continued to bounce as did the drop in Figure 3-4.

In Figure 3-7, a drop is observed impacting the 50% porous membrane at 230° C. The drop reached maximum flattening 7.9 ms after surface impact and no oscillations were visible after that point. The drop spread farther than did the drops in Figures 3-3 and 3-5. The contact angle  $\theta$  seen in frame four of Figure 3-7 is visibly smaller

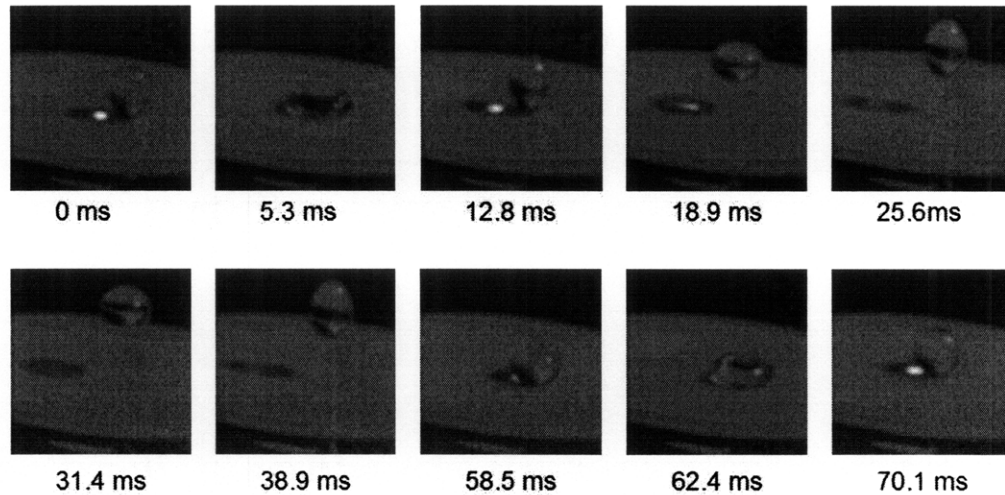


Figure 3-6: Film boiling was observed in the 40% porous surface above 220° C.

than that seen in frame six of Figure 3-5, indicating that the more porous surface is more wetting even at this higher temperature.

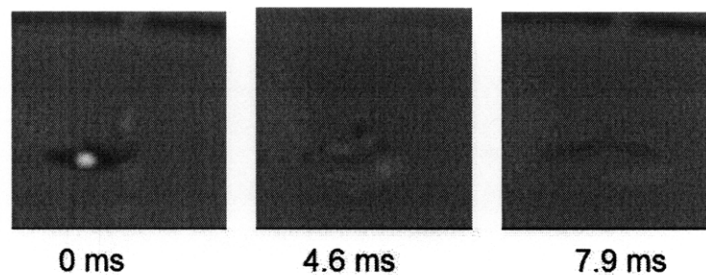


Figure 3-7: At 230° C, impinging drops wetted the 50% porous surface and no recoil was observed.

When the 50% porous membrane reached a temperature of 275° C, the impinging drops evaporated via film boiling, as shown in Figure 3-8. The drop flattened at nearly the same rate observed for the surface at 230° C, and became maximally flattened 7.2 ms after initial impact. During recoil, the drop left the surface 17.2 ms after initial impact and was levitated for 28 ms. Upon impacting the second time, the drop took 9.2 ms to spread to its maximum diameter.

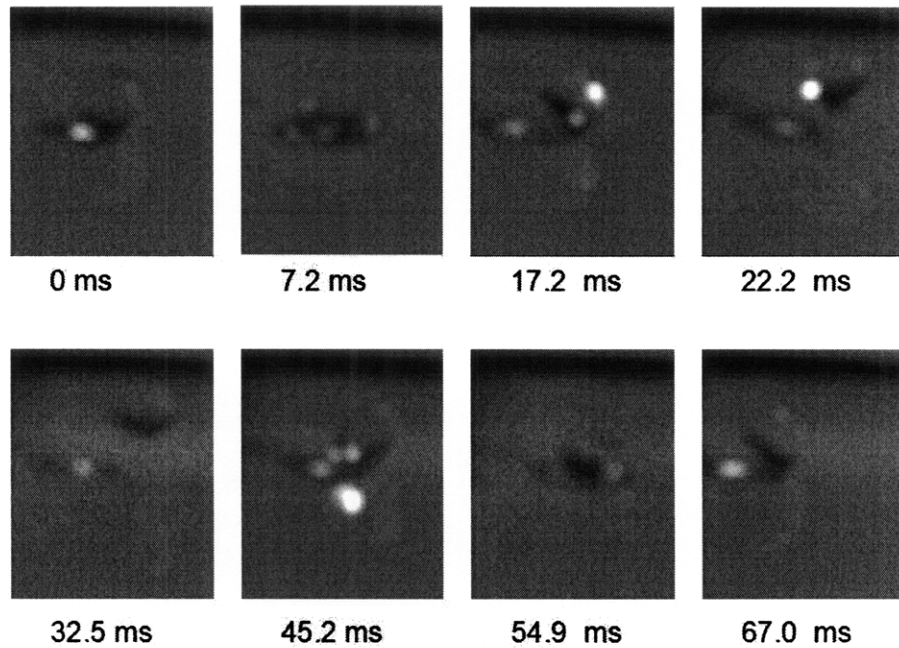


Figure 3-8: Drops impinging on the 50% porous surface at 275° C evaporated via film boiling.

### 3.4 Drops Impinging From a Height

Another important variable in the boiling of impinging droplets is the speed with which a drop impacts a superheated surface. Figure 3-9 depicts the progression of a drop released 15 cm above a silicon wafer heated to 200° C. Rather than expanding upon impact and then recoiling as a single drop, the drop is broken up into a central drop and many peripheral droplets. The increased speed at impact causes the drop to spread much more quickly than did the drops above. After the drop disintegrated, the larger central drop exhibited transition boiling while the smaller drops recoiled from the surface and evaporated via film boiling.

### 3.5 Chapter Summary

The experiments performed in this chapter demonstrated that the Leidenfrost temperature is influenced by surface porosity. The Leidenfrost point occurred 20° C higher

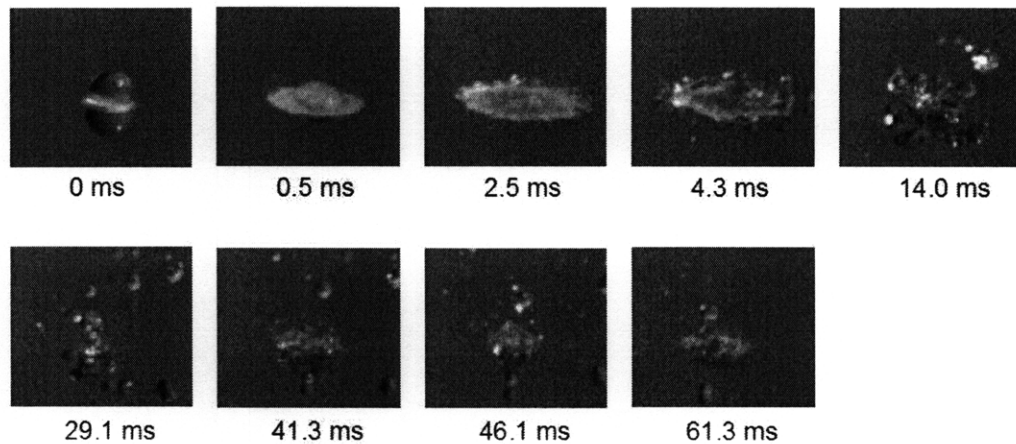


Figure 3-9: A drop impinging onto the silicon surface heated to 200° C quickly disintegrated.

on the 40% porous surface and over 45° C higher on the 50% porous surface. The differing surface conductivity and contact angle of silicon dioxide and aluminum oxide would not account for a difference of this magnitude, which can be attributed to the partial absorption of the vapor layer in the pores. These pores are isolated and therefore are not directly comparable to the microstructure modeled in Chapter 2. The regular array of posts does not divide the porous volume into distinct sections, but would allow vapor to flow continuously underneath the drop. Similarly drastic increases in Leidenfrost temperature should be achievable using such regular microstructures.

## Chapter 4

# Conclusions and Recommendations

In this thesis, the effect of a porous microstructure on the Leidenfrost temperature is explored. A one dimensional model of a regular, geometric microstructure indicated that optimum spacing and aspect ratios will result in a substantially higher Leidenfrost temperature for a given liquid-surface system. The optimum values of these ratios critically depends on the conductivity of the surface and vapor, vapor viscosity, the density of the vapor and liquid, the liquid surface tension and the contact angle between the surface and liquid. The achievable increase in Leidenfrost temperature also depends on these properties, but that limit has not been investigated.

Experiments in the boiling of water drops for surfaces of various porosities demonstrated a correlation between porosity and Leidenfrost temperature. A 40% porous surface exhibited a Leidenfrost temperature 20° C higher than that of a smooth surface, and an increase of over 45° C was observed for a surface of 50% porosity. These porous surfaces did not have a regular microstructure that could be simulated in the above model, but these results are promising.

If more time had been available, the boiling experiments of Chapter 3 would have been performed on the surfaces modeled in Chapter 2. These experiments would be most useful if combined with an expansion of the one dimensional model. The assumptions of laminar flow within the microstructure and pure conduction from the surface to the drop through the microstructure and vapor may not be valid for all microstructure geometries or surface temperatures. A systematic experimental study

of the effects of varying spacing and aspect ratio would validate the model developed here. A more complete model would also include the temperature variation of the liquid and vapor properties. This investigation would provide a thorough understanding of how a regular, repeatable microstructure can effect the Leidenfrost temperature, and could result in exciting applications in power production and microelectronics.



# Bibliography

- [1] C.T. Avedisian and J. Koplik. Leidenfrost boiling of methanol droplets on hot porous/ceramic surfaces. *International Journal of Heat and Mass Transfer*, 20(2):379–393, 1987.
- [2] John D. Bernardin and Issam Mudawar. A leidenfrost point model for impinging droplets and sprays. *Physics of Fluids*, 15(6):1632–1637, 2003.
- [3] John D. Bernardin and Issam Mudawar. A cavity activation and bubble growth model of the leidenfrost point. *Journal of Heat Transfer*, 126:272–278, 2004.
- [4] John D. Bernardin, Clinton J. Stebbins, and Issam Mudawar. Effects of surface roughness on water droplet impact history and heat transfer regimes. *International Journal of Heat and Mass Transfer*, 40(1):73–88, 1997.
- [5] John D. Bernardin, Clinton J. Stebbins, and Issam Mudawar. Mapping of impact and heat transfer regimes of water drops impinging on a polished surface. *International Journal of Heat and Mass Transfer*, 40(2):247–267, 1997.
- [6] Anne-Laure Biance, Christophe Clanet, and David Quere. Leidenfrost drops. *Physics of Fluids*, 15(6):1632–1637, 2003.
- [7] H. Bostanci, D.P. Rini, J.P. Kizito, and L.C. Chow. Spray cooling with ammonia on micro-structured surfaces: Performance enhancement and hysteresis effect. 2008.
- [8] Cheng-Chieh Hsieh and Shi-Chune Yao. Evaporative heat transfer characteristics of a water spray on micro-structured surfaces. *International Journal of Heat and Mass Transfer*, 49:962–974, 2006.
- [9] G.P. Peterson. *An Introduction to Heat Pipes: Modeling, Testing, and Applications*. Wiley Series in Thermal Management of Microelectronic and Electronic Systems. Addison-Wesley, John Wiley and Sons, first edition, 1994.
- [10] SPI Supplies. Anopore inorganic aluminum oxide membrane filters. [http://www.2spi.com/catalog/spec\\_prep/filter2.shtml](http://www.2spi.com/catalog/spec_prep/filter2.shtml), May 2009.
- [11] Kripa K. Varanasi, Tao Deng, Ming F. Hsu, and Nitin Bhate. Design of superhydrophobic surfaces for optimum roll-off and droplet impact resistance. In *Proc. ASME International Mechanical Engineering Congress and Exposition*.